Zeitschrift: Helvetica Physica Acta
Band: 52 (1979)
Heft: 2

Artikel: The use of high-density proportional chambers for positron annihilation studies in aluminium and copper
Autor: Manuel, A.A. / Samoilov, S. / Fischer, Ø
DOI: https://doi.org/10.5169/seals-115030

Helvetica Physica Acta, Vol. 52 (1979), Birkhäuser Verlag, Basel

The use of high-density proportional chambers for positron annihilation studies in aluminum and copper

A. A. Manuel, S. Samoilov, Ø. Fischer and M. Peter

Département de Physique de la Matière Condensée
Université de Genève CH-1211 Genève 4

and

A. P. Jeavons

CERN, CH-1211 Genève 23

(3. IV. 1979)

Abstract. A bidimensional positron annihilation angular correlation system is presented. It is equipped with high-density proportional chambers. The characteristic properties of the experimental setup are described, as well as measurements on aluminum and copper. Information obtained about the Fermi surface topology, the core annihilation momentum distribution, the umklapp processes and the many body effects in those metals are discussed.

Introduction

The positron annihilation method has been used, for quite some time, in the study of Fermi surfaces (*FS*) in metals (1). In the last years (2), this field has evolved with the advent of two dimensional (2-D) systems.

Positrons emitted by a radioactive β^+ source strike the surface of the investigated sample. In metals, the positron is thermalized (3) prior to its annihilation with an electron. The annihilation process yields, in most cased, two γ-rays carrying mainly the momentum $\vec{p}$ of the annihilated electron. Linear momentum conservation implies then a small angular deviation from 180°, $\theta = p/mc$, typically some milliradians (mrad), of the two γ-rays. Therefore, the angular correlation of the two photon annihilation radiation carries the information concerning the electronic momentum distribution in the sample.

In the independent particle approximation the probability for a two photon annihilation process carrying momentum $\vec{p}$ is proportional to:

$$\rho(\vec{p}) \div \sum_{\vec{k},l} n_{\vec{k},l} \left| \int \exp(-i\vec{p}\cdot\vec{r})\psi_+(\vec{r})\psi_{\vec{k},l}(\vec{r})\, d^3\vec{r} \right|^2$$

$$\div \sum_{\vec{k},l} n_{\vec{k},l} \sum_{\vec{G}} \delta(\vec{p} - \vec{k}\vec{G}) |A_{\vec{G}}(\vec{k}, l)|^2 \qquad (1)$$

where $\psi_+(\vec{r})$ is the positron ground state wave function, $\psi_{\vec{k},l}(\vec{r})$ is the electron wave for wave vector $\vec{k}$ and band index l and $n_{\vec{k},l}$ is the occupation number of the

state $(\vec{k}, l)$. The $\vec{G}$ are reciprocal lattice vectors and the $A_{\vec{G}}(\vec{k}, l)$ are the Fourier components:

$$A_{\vec{G}}(\vec{k}, l) = \int_{\text{cell}} \exp(-i(\vec{G}+\vec{k})\cdot\vec{r})\psi_+(\vec{r})\psi_{\vec{k},l}(\vec{r})\, d^3\vec{r} \tag{2}$$

Thus each electron with wave vector $\vec{k}$ contributes to the annihilation rate not only at $\vec{p}=\vec{k}$, but at every $\vec{p}=\vec{k}+\vec{G}$, with relative intensity $|A_{\vec{G}}(\vec{k}, l)|^2$. The contributions with $\vec{G}\neq 0$ are called the high momentum components (HMC) or Umklapp processes.

One sees from equation (1) that all occupied bands will contribute to $\rho(\vec{p})$, depending on the overlap between the positron and electron wave functions in real space. The positron being a positively charged particle, it will have a null wave function at the atomic sites and maximal in the interstitial region. Thus the two major contributions to $\rho(\vec{p})$ are the annihilations with the valence electrons, corresponding to $\vec{G}=0$, which carry the information concerning the FS topology, and the ones with the core electrons. The relative intensities of those contributions depend crucially on the overlap between the wave functions. The contribution to $\rho(\vec{p})$ from occupied valence states is continuous up to the Fermi wave vector $\vec{k}_F$. At $\vec{k}_F$ a discontinuity is expected. It will manifest itself most clearly in the derivative. Therefore, information concerning the FS topology may be obtained from a careful study of those breaks in the momentum distribution.

A positron in a metallic environment is a "dressed" particle, surrounded by a cloud of electrons, therefore its effective mass is higher than its free mass, depending on the environment. Obviously, in such a situation, the many body effect interactions will have an influence on the momentum distribution. For a free electron gas (4), those interactions result in an enhancement factor having the following expression:

$$E(\gamma) = A + B\cdot\gamma^2 + C\cdot\gamma^4; \qquad \gamma = k/k_F. \tag{3}$$

For real metals the question is still not resolved. In a bidimensional measurement (5), two components of the pair momentum are resolved, namely p_x and p_y. Therefore the measured angular correlation distribution is given by:

$$N(p_x, p_y) = \int \rho(\vec{p})\, dp_z \qquad p_x = mc\theta_x; \quad P_y = mc\theta_y \tag{4}$$

where θ_x and θ_y are the resolved angular components.

In Section A, we describe the bidimensional experimental setup used in this work, its characteristic properties and the algorithms used for the phenomenological data analysis. In Section B the measurements on aluminum and copper are presented, including a detailed analysis of the FS topology, the core annihilation contribution, the HMC contributions and the many body effects.

Section A—Experimental setup

1. *Description*

The experimental setup (6) used in this work consists of a dewar where the sample and the positron source are located, two bidimensional detectors,

electronic hardware and a computer which monitors the data acquisition and performs a preliminary numerical treatment of the coincident events.

The dewar is a standard liquid helium dewar equipped with a gas exchange compartment. Thus the sample temperature may be varied from 4.2 K to 300 K continuously.

The positron source is about 30 mCi of ^{22}Na with an active area of 10 mm × 1 mm. The monocrystalline sample is placed 4 mm above the source. Typical sample size is 10 mm × 1 mm for the surface facing the source, and 3 mm height. The long edge of the sample is parallel to the detector-detector axis. The source is collimated by two cylindrical gold collimators, 37 mm long each, having a hollow axis of 4 mm in diameter for the outcoming annihilation radiation. Thus, no direct radiation from the source reaches the detectors. Moreover, in the path of the γ-rays towards the detectors, the dewar is equipped with 0.2 mm thick windows to avoid scattering. The sample-detector distance is 4.485 ± 0.005 m.

2. *The detectors*

The detection of the incident γ-radiation is performed by means of two high-density proportional chambers (HDPC) (7) (Fig. 1).

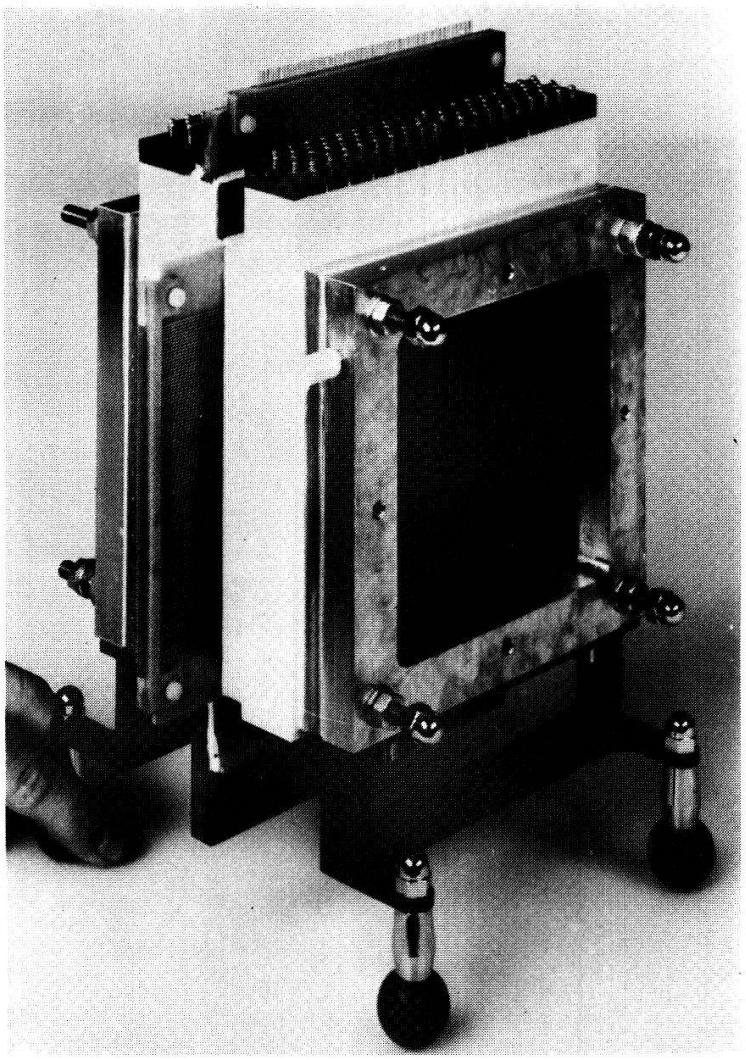

Figure 1
A high-density proportional chamber. The multiwire chamber is located between the two (white blocks) converters.

It is well known that a conventional proportional chamber is not efficient for 511 KeV γ-rays. In order to stop this radiation a high-density material is needed. On the other hand, in positron annihilation physics a good spatial localization is primordial. This is the characteristic property of a multiwire proportional chamber (MPC). The combination of these two requirements led to the realization of our detectors.

Essentially it is a MPC placed between two high-density γ to electron converters (Fig. 2). Each converter is made of 75 sheets of lead-bismuth alloy $12 \times 12\ cm^2$ in surface and 0.25 mm thick, separated by 74 sheets of glass-fibre epoxy-resin with the same area and 0.1 mm thick. The central $10 \times 10\ cm^2$ area of each converter is drilled with 10^4 cylindrical channels 0.8 mm in diameter, in a hexagonal closely packed geometry with 1 mm pitch. Each metallic sheet is brought to a different potential, by means of a voltage divider, to create an electric field of about 2 kV/cm in the channels. The two converters are slightly shifted one in respect to the other so that the channels do not coincide: when a γ-ray passes through the first converter without interacting the second may stop it. Hence, the detection efficiency is increased.

When a γ-ray strikes the lead-bismuth alloy an electron can be emitted, due to the Compton or photoelectric effects. This electron has a significant probability to emerge into the nearest channel of the converter, due to the deliberately chosen geometry (8). Once in a channel, it ionizes the gas and the resulting electrons are drifted by the electric field into the MPC.

The MPC is made of three planes of wires (Fig. 3). The central plane, the anode, is made of gold plated tungsten wires of 20 μm in diameter with a spacing of 1.73 ± 0.03 mm. The spacing was so chosen that each wire is directly in front of a vertical (y) series of channels in the converter. The wires potential is 3.8 kV, corresponding to the region of proportional response of the chamber. On both sides of the anode plane are the cathode or read-out planes, maintained at zero voltage. They are made of 96 bronze-beryllium wires of 100 μm in diameter, the spacing being 1 ± 0.03 mm. The gap between each cathode plane and the anode

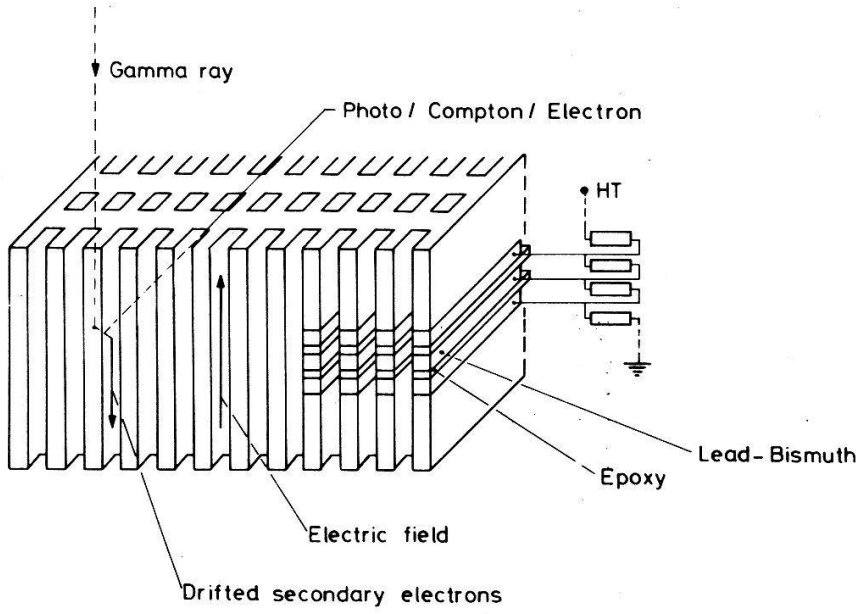

Figure 2
The gamma to electron converter.

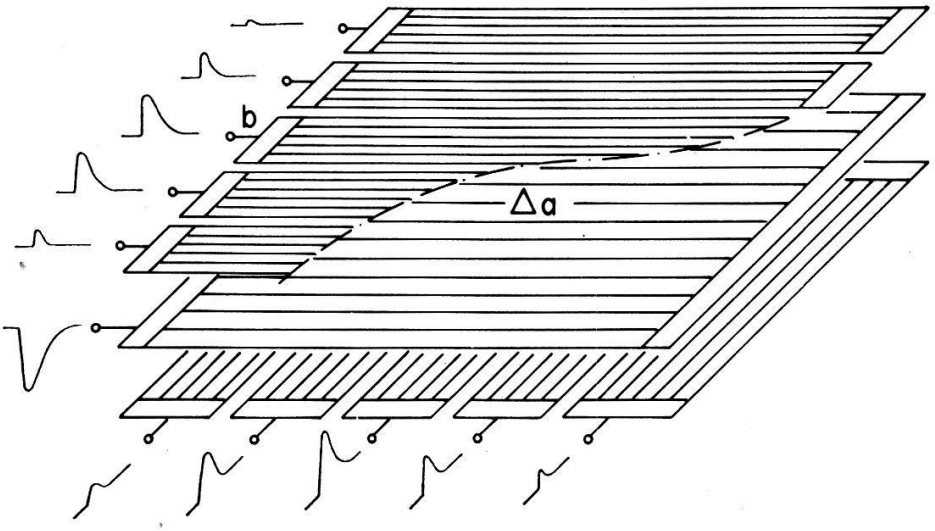

Figure 3
The multiwire planes.

plane is 3 mm. The wires of the cathode planes are in perpendicular directions, x and y respectively.

Whenever drifted electrons are in the vicinity of an anode wire, they are accelerated by the very high electric field and ionize the gas. An avalanche is produced and the initial charge is amplified (9). The electrons reach the anode very quickly, but their contribution to the induced pulses on the cathode is weak. It is the heavy gas ions, repulsed from the anode, which produce the distribution of pulses of varying amplitude detected on each read-out plane (Fig. 3). The centres of gravity of these distributions determine the bidimensional coordinates of the relative impact of the incoming γ-ray.

The gas in such detectors should have the following properties: first, a high drift velocity for the electrons in the converter, in order to minimize the coincidence resolving time, secondly, big enough charge amplification in the avalanche prosess, in order to obtain pulses of sufficient amplitude. After many trials, pure isobutane (C_4H_{10}) was chosen. It has a relatively good stopping power for fast electrons: 6.5 KeV/cm for 0.5 MeV electrons, compared to 3 KeV/cm in argon. A high charge amplification is obtained, 10^4-10^5 in the proportional region. The drift velocity for slow electrons (0.5 eV) is 5 cm/μsec. This determines the coincidence resolving time as 400 nsec.

3. *Electronic hardware and data acquisition*

Every four wires of the cathode planes are grouped together and connected to a charge sensitive amplifier followed by a voltage amplifier and an analog to digital converter (*ADC*). Thus there are 24 electronic channels per read-out plane. The sum of the pulses of one whole cathode plane per detector is used as the initial trigger for the detection of an event.

The coincidence trigger logic and the corresponding timing diagram are shown in Fig. 4. Whenever the peak of the sum pulse is bigger than a threshold (30 mV), the pulse digitalization for each channel begins. After 500 nsec, a fast clear is sent to the *ADC*'s unless a coincidence is detected. In the latter case, the fast clear command is inhibited during the time (1–6 msec) needed to analyse the coincident event by software.

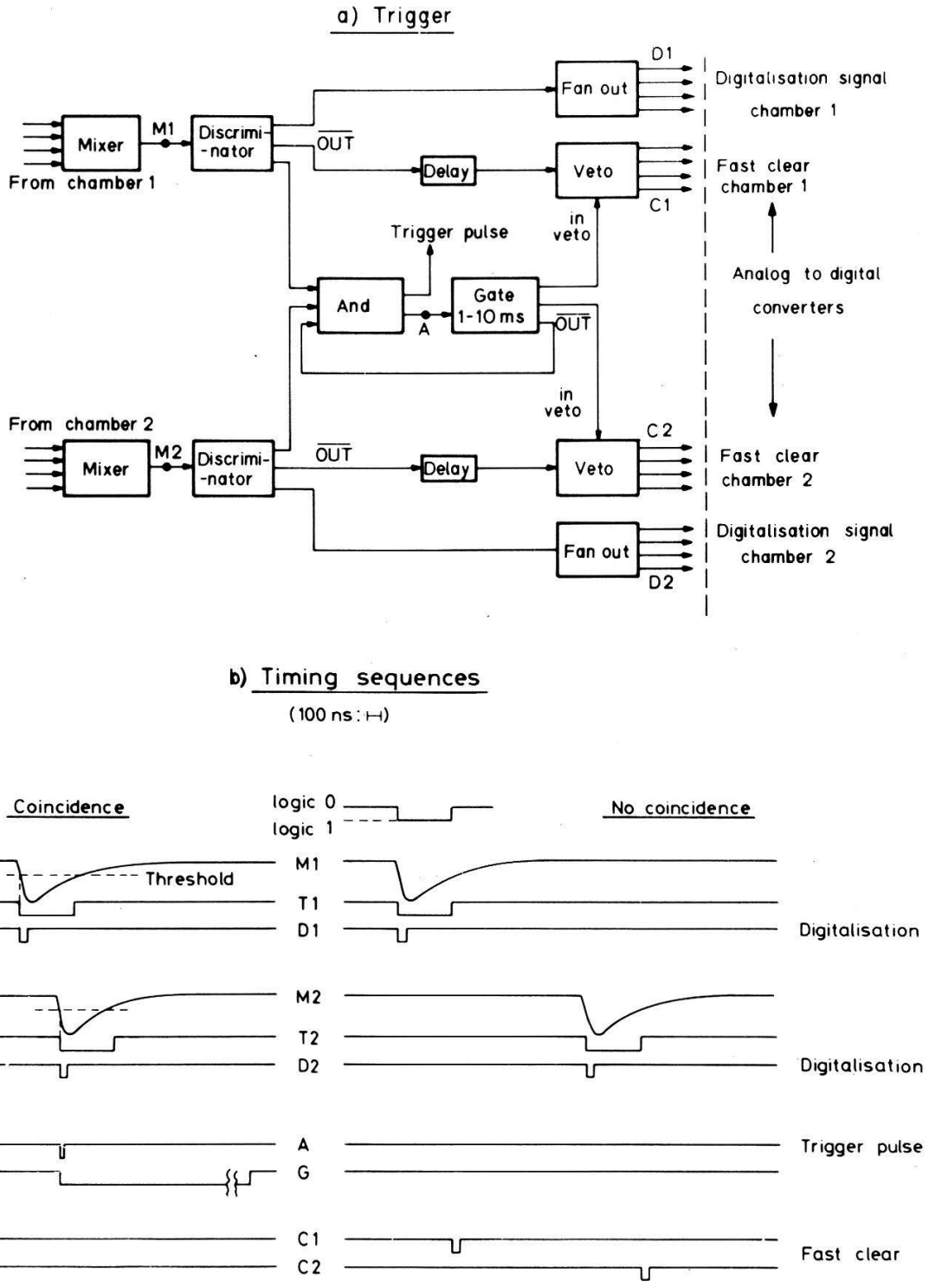

Figure 4
The coincidence trigger logic and timing diagram.

The data is sent through a CAMAC system to a PDP 11/40 computer which supervises the whole data acquisition process, performs a preliminary treatment on coincident events and stores the accepted information on disc or magnetic tape. A schematic diagram of the digital system is shown in Fig. 5.

The preliminary treatment consists, first, in testing the validity of the information. An event in coincidence is rejected if there is some probability that it is due either to noise or to an abnormal response of the MPC, such as in the case of an energetic cosmic ray. An event is rejected if one of the following features is

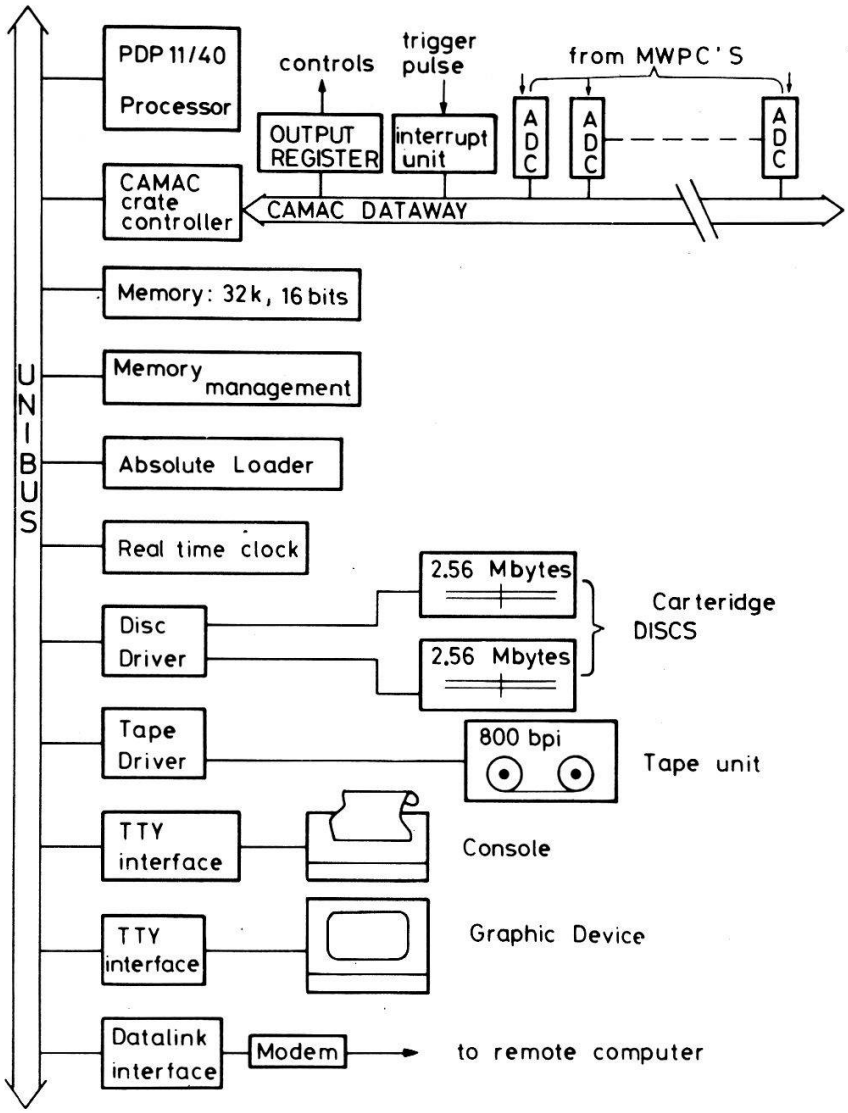

Figure 5
Schematic diagram of the digital system.

detected in the pulse distribution, in any one of the four read-out planes:
- one of the pulses overloads its ADC
- more than one set of contiguous pulses is present above the threshold (noise or Compton scattering in the converters)
- the number of pulses is smaller than 2 (in that case the centre of gravity is meaningless), or greater than 7 (abnormal response)
- the sum of the pulse height in the distribution is greater than an upper limit (abnormal response) or smaller than a lower limit (noise limit)

About 25% of the detected events in coincidence are rejected by software. For the remaining, the centres of gravity (x_1, y_1, x_2, y_2) of the digitalized pulse distributions for each read-out plane are computed. It is done in units of $\frac{4}{9}$ mm. Consequently a centre of gravity is an integer number in the range of 1 to $9 \cdot 24 = 216$. Thus, the four centres of gravity occupy 4 bytes.

4. *Characteristic properties of the experimental system*

(a) *The spatial resolution*

The spatial resolution of the detectors is not the same in both directions. An avalanche is constrained to occur in the close vicinity of a high voltage wire of the

anode plane. Therefore, in the direction perpendicular to those wires (x), the spatial distribution is expected to have a period of 1.73 mm, the spacing between the wires. Figure 6a shows the spatial distribution of events in the x direction when a uniform flux of γ-rays hits the detector. The positions of the anode wires are clearly reflected.

In the direction parallel to the anode wires (y) it seems at first sight that the spatial distribution should be homogeneous. It is not the case, a periodic structure appears with a period of 1 mm (Fig. 6b), but, much less pronounced than in the x direction: the electrons coming from the converters are deviated by the cathode wires and the distribution of the avalanches on the corresponding anode wire will have a period of 1 mm in the y direction (Fig. 6c).

As for the spatial resolution, in the x direction, the 1.73 mm spacing between the high voltage wires is predominant so that it is close to a square function of 1.73 mm in width. In order to measure more precisely the spatial resolution in the y direction we tried to obtain the image of a narrow (0.5 mm) slit in a 50 mm thick block of lead, in front of which is placed a 2 mCi point source of ^{22}Na. The response of the detector, corrected for the spatial resolution in the y direction (Fig. 6b), is shown in Fig. 7. Some care must be taken in analysing this result since, in the proposed experiment, the point source is placed close to the detector and the parallax effect due to the converters has to be taken into account. Therefore, it is fitted numerically by a convolution between the geometry of the slit (taking into account the absorption in lead) and both converters, with a Gaussian function assumed to represent the spatial resolution. The only free parameter is the *FWHM* of this Gaussian. The best fit (solid line in Fig. 7) is obtained for a *FWHM* of 1.7 ± 0.1 mm.

(b) *The angular resolution*

The angular resolution is obviously a function of the detector-sample distance. Therefore only the distance of 4.485 m will be considered in the following.

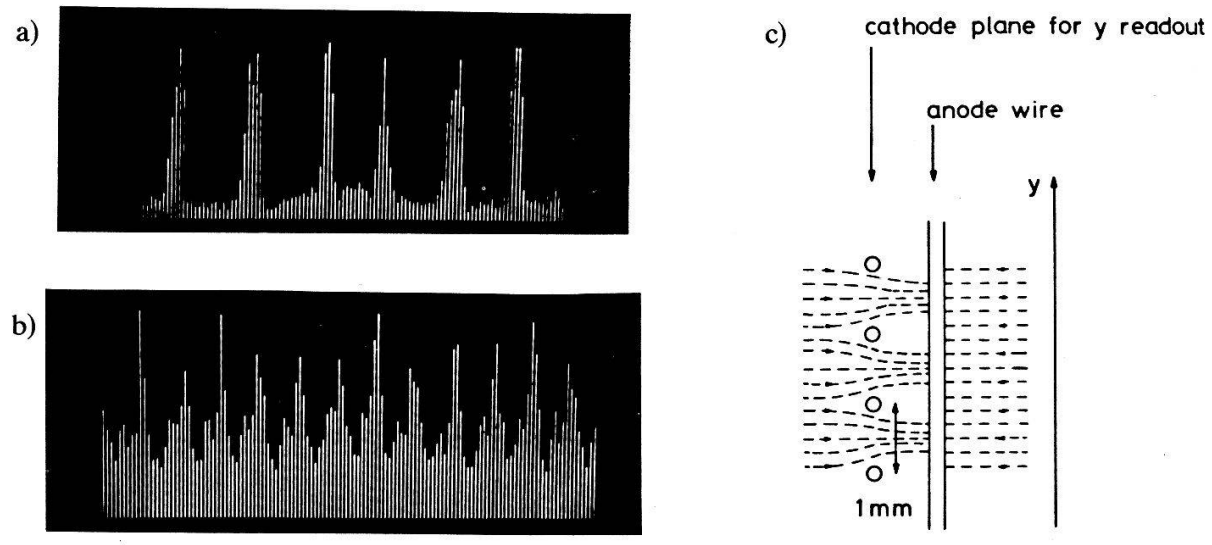

Figure 6
The spatial distribution in (a) the x direction (b) the y direction, for a uniform incoming flux of radiation. 1 channel = 1/10 mm; (c) electric flux lines in the y direction, in the vicinity of the anode and cathode wires.

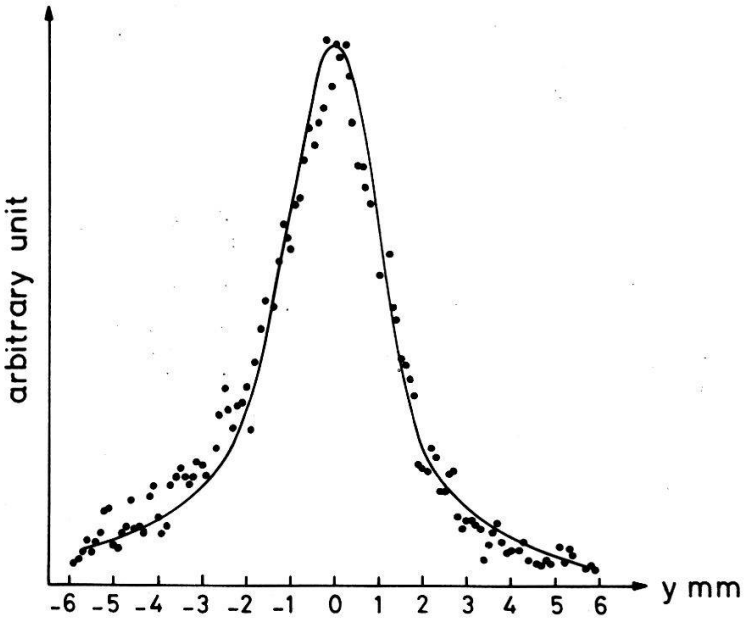

Figure 7
The image of a narrow horizontal slit (0.5 mm). The solid line represents (see text) a Gaussian fit for the spatial resolution in the y direction. The FWHM is 1.7 mm.

The effective angular resolution is a convolution of the spatial resolution of both detectors and the thermal positron momentum at a certain temperature T. In the x direction only, a further convolution is necessary due to the sample width (in the y direction, the positron penetration depth is at most 10 μm (10), therefore negligible). In a metal one can assume that the positron thermal momentum has a Boltzmann distribution:

$$F_+(p) = A \exp(-p^2/2m^* k_B T) \tag{5}$$

where $m^* = \alpha m_0$ is the positron effective mass in the sample. Assuming that $\alpha = 2$ (11), Fig. 8 shows the effective experimental angular resolution as a function

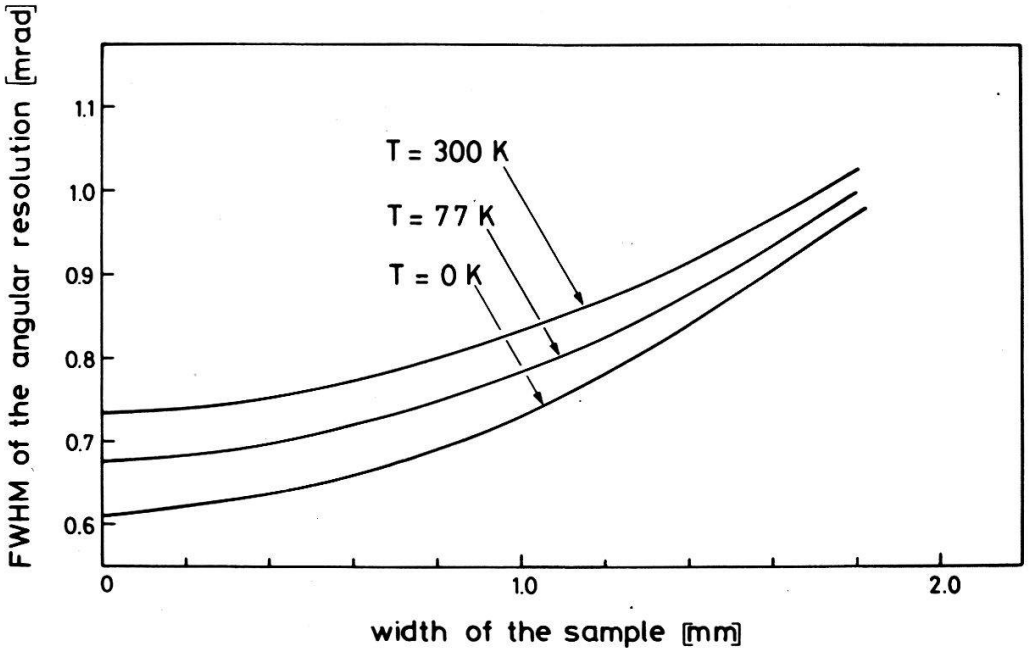

Figure 8
The effective angular resolution.

of sample width (x direction only) for different temperatures. Thus, with a sample of 1.0 mm wide, at 77 K, the angular resolution is 0.78×0.68 mrad^2.

(c) *The detector efficiency and the signal to noise ratio*

It is very difficult to measure those parameters. The detectors do not have any resolution in energy and their efficiency is energy dependent, increasing with energy. We tried to measure directly the efficiency by performing the same coincidence measurement twice. Once with two standard NaI detectors and once when one of the NaI detectors is changed for a HDPC. The result is:

$$\varepsilon = 0.1 \pm 0.03$$

As for the signal to noise ratio, it is even more difficult to estimate from the first principles, since we do not know the intensity of the incoming flux, about 25% of the events in coincidence are rejected by software and the analysis time for an acceptable event may be up to 6 msec which is not negligible. Thus, theoretically it is a complicated pile-up of stochastic processes. Therefore we estimated the signal to noise ratio from the experimental data which will be presented in Section B. The result is $S/R = 15$.

5. *Data analysis*

(a) *The angular efficiency function*

For each recorded event the respective angles θ_x and θ_y are computed on the basis of the centres of gravity. This transformation implies an angular efficiency function due to the finite size of the detectors. For linear and perfectly homogeneous detectors of size L and detector-sample distance d, the angular efficiency function is a triangle of base $2\delta = 2L/D$: it is maximal for $\theta = 0$ and null for angles bigger than $\pm\delta$. For perfectly homogeneous 2-D detectors, the theoretical angular efficiency function is close to a pyramid. But, with concave faces instead of planar ones. Its base is square if the detectors are square. Its peak is truncated if one of the detectors is bigger than the other or if two identical detectors are placed at different distances from the sample (12).

The real angular efficiency function depends on the degree of homogeneity of the detectors and, to some extent, on the precision of the computation of the centres of gravity, for instance the integer truncation may induce a slight step like character. Therefore, the optimal solution is to measure this function experimentally. It can be done by using an anticoincidence trigger for the radiation coming from the sample. Figure 9 shows a typical histogram representing the angular efficiency function. It contains the basic information needed to correct the raw data.

(b) *The histograms of the angular correlations*

For each measurement an histogram of the angular correlations is computed from the registered centres of gravity and, subsequently, corrected for the

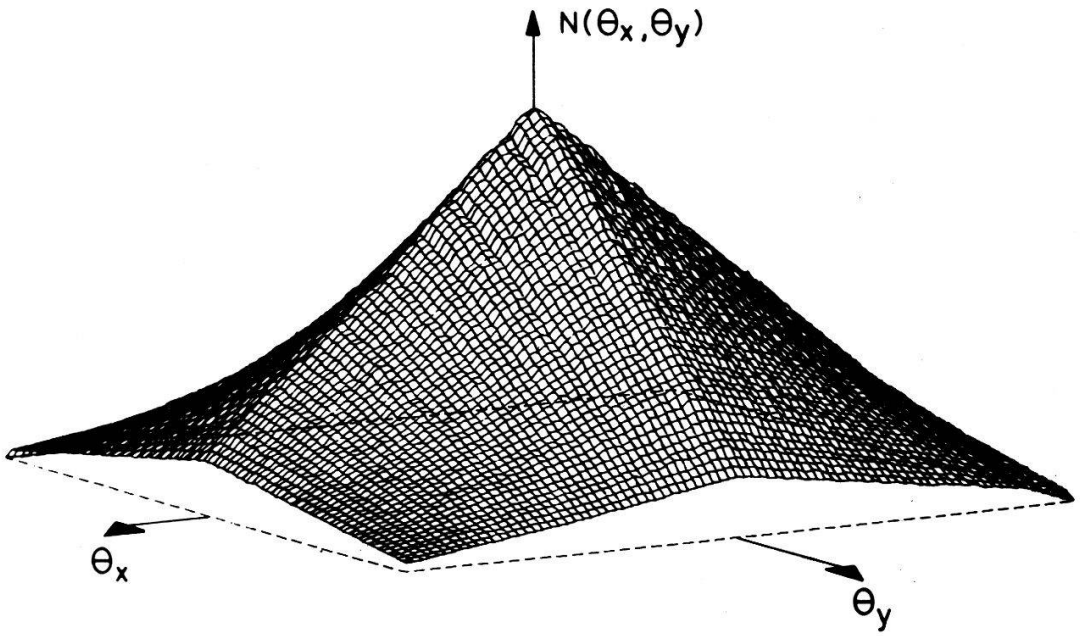

Figure 9
The angular efficiency function.

efficiency function. Finally, an histogram of 104×104 channels of 0.396×0.396 mrad^2 each is obtained. This is our basic histogram on which the final data analysis is performed.

The step of 0.396×0.396 mrad^2 is less than our angular resolution. We have a further degree of freedom which consists in adding the number of counts $N \times M$ channels and obtaining an histogram of 104×104 channels of $0.396N \times 0.396M$ mrad^2 each. We shall refer to such an histogram in the following as a "binned $N \cdot M$" histogram. This procedure proved to be useful for the study of the *HMC* at large angles where the main handical is poor statistics.

In some cases it is more convenient to begin the analysis on a one dimensional angular distribution, for instance to get a rough estimated of the most critical parameters. This may be obtained by integrating the 2-*D* data over x for instance. The result will be denoted in the following by the "long-slit distribution" in the y direction.

(c) *Basic data analysis procedures*

The following software was developed for the analysis of the data:

- three dimensional visualisation of any two dimensional histogram, using the method of axonometric projection
- isodensity contour lines mapping of any two dimensional histogram
- the computation of the partial derivatives $\partial N(\theta_x, \theta_y)/\partial\theta_x$ for any θ_y and $\partial N(\theta_x, \theta_y)/\partial\theta_y$ for any θ_x. Two algorithms are used. One consists in taking slices of the angular histogram and computing the difference between the number of counts of two experimental points distant 0.792 mrad from each other, for a given slice. It is very rapid but the derivative is noisy. The second, fits a second order polynominal to each four consecutive points in a slice, and, the derivative is computed at predetermined points falling in the interval of the two central

points out of the four. Those partial derivatives are very useful for the determination of the *FS* topology, since the momentum distribution should show a discontinuity at k_F

- a general numerical fitting procedure based on the non-linear least squares method (*LSQF*). It permits to obtain a rapid rough eatimated of the parameters, which are then used as initial estimates for a final convergence. The fit is submitted to a χ^2 test, thus for a given confidence interval the likelihood between the experimental data and the theoretical model is tested.

Section B—Measurements

1. *Aluminum*

We endeavoured this measurement in order to check the reliability of the experimental setup. The choice of aluminum as a test case was made for those reasons. It is a simple trivalent metal, nearly free electron (*NFE*) like, which exhibits a relatively low intensity board momentum distribution due to core annihilations on which is superimposed a prominent almost spherical distribution due to annihilations with the valence electrons (1, 13, 14).

The aluminum single crystal (6) was grown for the liquid phase using the Czochralski technique. The initial material had a 5N purity. The sample was cut by spark erosion, chemically etched, annealed in vacuum for 24 hours at 560°C, slowly cooled down and finally chemically etched again. Its dimensions were 12 mm long and 1.2 mm wide. The [100] plane faced the radioactive source with the [100] and [010] axes along θ_x and θ_y respectively. The measurement was performed at 77 K, corresponding to an effective angular resolution (Fig. 8) of 0.82×0.68 mrad^2.

The experimental result is shown in Fig. 10. The spacing between two lines in the histogram, in both directions, is 0.396 mrad. The normalization was so chosen that the almost spherical topology of the *FS* is exhibited. The projective representation of the partial derivative $|\partial N(\theta_x, \theta_y)/\partial\theta_x|$, obtained from differences, is shown in Fig. 11. The sharp cut off at k_F is certainly the dominant feature.

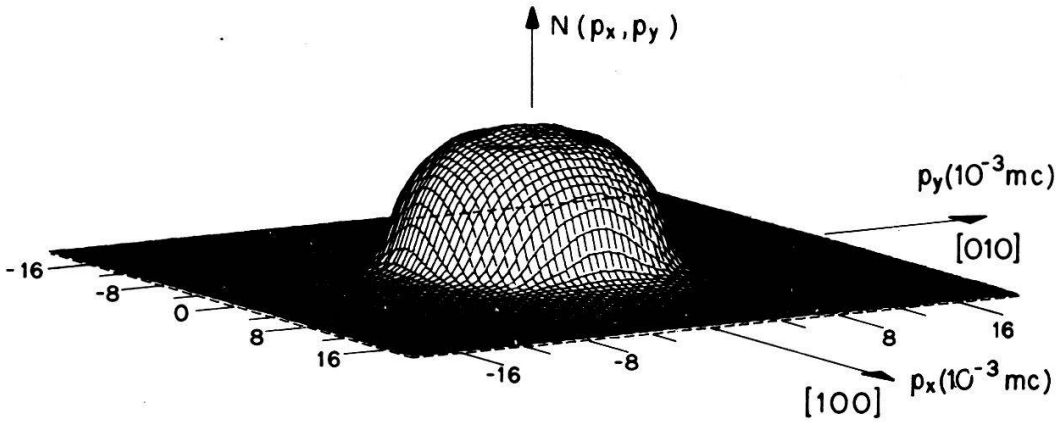

Figure 10
The bidimensional angular distribution in aluminum.

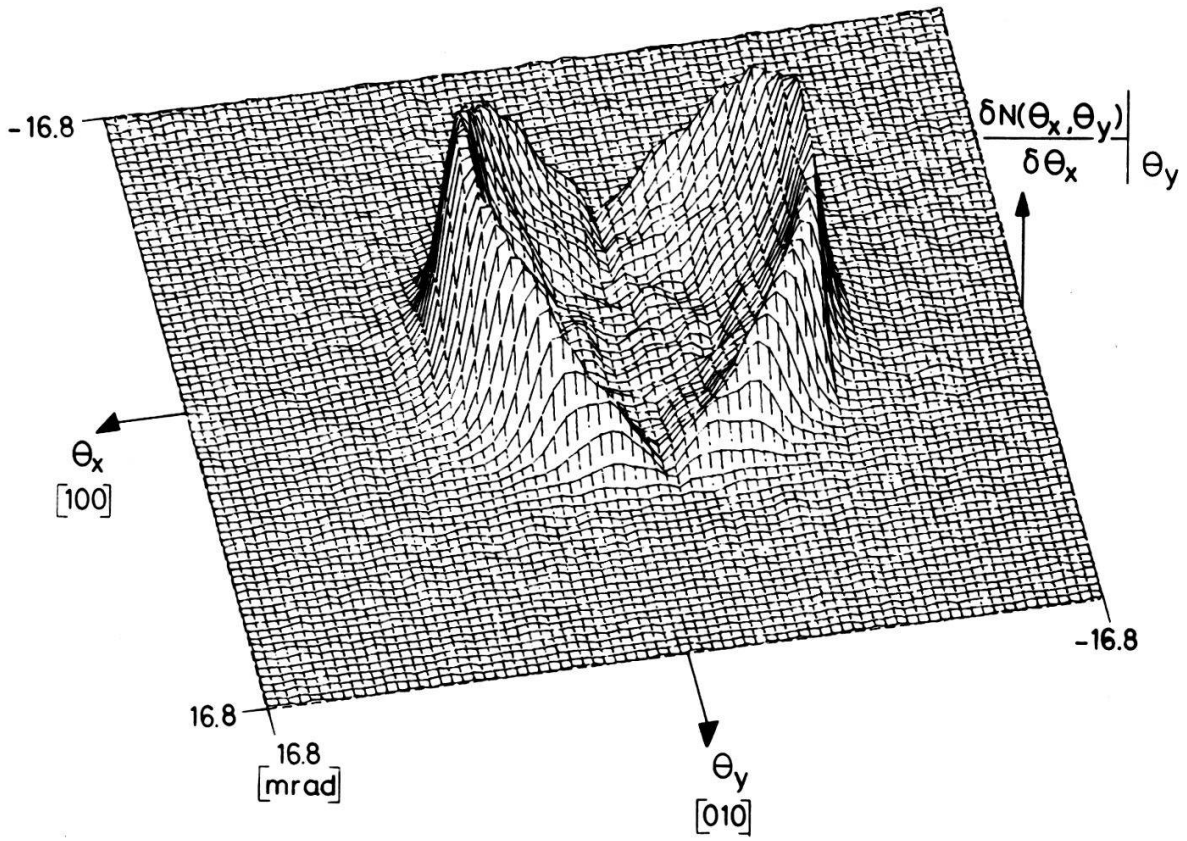

Figure 11
The projective representation of the partial derivatives $|\partial N(\theta)/\partial\theta_x|$ in aluminum.

The quantitative analysis was done progressively in three stages. In the first one, the aim was the evaluation of k_F taking into account the resolution. This was done on the long slit distributions in the [100] and [010] directions. The derivatives were computed by means of second order polynomials (Section A-5c) and fitted numerically by the *LSQF* procedure. The theoretical model is based on a free electron sphere of radius k_F (integration of the Fermi function), to which a Gaussian distribution representing the core annihilation is added, and, the whole convoluted with a Gaussian resolution function. The best fit confirmed our estimation (Section A-4b) for the effective angular resolution in both directions, and, yielded the value of 6.79 ± 0.1 mrad for k_F. This is in agreement with the theoretical value of $k_F = 6.78$ mrad for a free electron gas having the aluminum electron density.

The next step consisted in fitting the whole 2-*D* spectrum. The model function, still based on the free electron approximation was:

$$F(x, y) = r + C_0 \exp(-x^2/2\sigma_x^2) \cdot \exp(-y^2/2\sigma_y^2) + A(R^2 - x^2 - y^2)^{1/2} \cdot E(\gamma) \cdot D(\gamma) \quad (6)$$

where the first term represents the random coincidences, the second the core annihilation and the third the annihilation with the valence electrons including two corrections due to the many body effects. $E(\gamma)$ is a Kahana (4) type of enhancement factor:

$$E(\gamma) = 1 + U \cdot \gamma^2 + V \cdot \gamma^4; \qquad \gamma = k/k_F \leq 1$$

$D(\gamma)$ is a Daniel and Vosko (15) type of many body interaction. For $\gamma > 1$ the

asymptotic behaviour is:

$$D(\gamma) = \eta\gamma^{-8}$$

This model function is then convoluted with the known effective angular resolution of $0.82 \times 0.68\ \text{mrad}^2$.

The parameters of this simple model (r, C_0, σ_x, σ_y, A, R, U, V, D) were obtained by the *LSQF* method in two steps. In the first, a rapid minimalization of χ^2, using the whole histogram, yielded for a slow and final minimalization of χ^2, using that time only a quarter of the experimental data. The results are the following (experimental spectrum normalized to 1):

- The random coincidences ($R = 0.01$) represent 1% of the maximal number of counts.
- The 2-D gaussian, assumed to describe the core annihilation, has an amplitude of $C_0 = 0.10$ and a standard deviation of $\sigma_x \simeq \sigma_y = 7.4 \pm 0.3$ mrad (in fact the best fit yielded $\sigma_x \simeq \sigma_y$ within the error).
- The Fermi wavevector $k_F = R = 6.78$ mrad in agreement with the derivative fit and the free electron value.
- The parameters of the Kahana enhancement factor are:

$$U = 0.132\ (0.172) \qquad V = 0.017\ (0.116)$$

compared to the theoretical values, in brackets, for a free electron gas at *OK* (4). This result suggests that the many body effects are less pronounced in a *NFE* metal like aluminum than in a free electron gas having the same electronic density.

- The parameter of the Daniel and Vosko type of interaction $\eta = 0.21$. This result is surprisingly high, but it affects only a very limited region due to the γ^{-8} dependence in k.

In this model, the *HMC* processes were ignored. The reason is technical. The addition of, at least, two more parameters, which are in competition during the *LSQF* with the already present ones, has a disastrous effect on the computing time per iteration and the convergence is doubtful. But, their conclusion can only reduce the many body effects parameters, strengthening our previous conclusion. On the other hand, they might be the reason for the high value obtained for η. Nevertheless, the *HMC* are too weak to wash-out the tail for $k > k_F$. It is certainly needed in order to fit our experimental data. Kubica and Stewart (16) were confronted with the same problem in manganese and introduced a linear tail above k_F.

The study of the *HMC* was done on a binned 3×3 histogram. In Fig. 12 is shown the corresponding isodensity contour lines mapping, as well as the positions of the first Brillouin zone (*BZ*), the eight nearest neighbouring *BZ* (*NNBZ*) corresponding to the reciprocal lattice vector $G = 2\pi/a\{1, 1, 1\}$, and, the six second neighbouring *BZ* corresponding to $G = 2\pi/a\{2, 0, 0\}$. The 6% and 8% contour lines exhibit clearly maximums at the centres of the *NNBZ* and minimums in between. Obviously, the centre of a *NNBZ* and the intersection point (Fig. 12) between the line AC and the circle centered at A of radius AB, are equivalent except for the *HMC* contribution. A careful comparison between

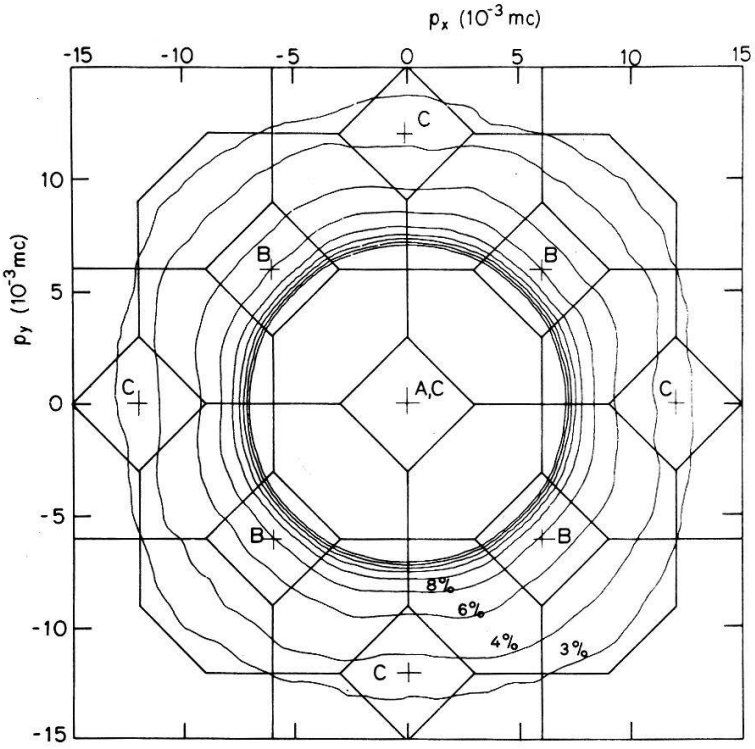

Figure 12
Isodensity contour lines mapping of a binned 3×3 histogram in aluminum. The deviations from circles are attributed to umklapp processes (see text).

the intensities of such equivalent points yielded the following result for the Fourier components $A_{\vec{G}}(\vec{k}, l)$ of equation (2):

$$|A_{\{111\}}(\vec{k}, l)|^2 = 0.03 \pm 0.01$$
$$|A_{\{200\}}(\vec{k}, l)|^2 = (0.006 \pm 0.1) = 0$$

This result is a quantitative estimate of the deviation from free electron behaviour.

Aluminum has three valence electrons per atom, thus the first *BZ* is full and the third and fourth zones are practically empty. In the reduced zone scheme, the second zone is occupied by 0.98 electron per atom. In the *NFE* approximation this implies a deviation from free electron behaviour at the zone boundaries. Obviously, this interaction will be the best observed at the points *W* of the *BZ*, where the zone boundary is the closest to the *FS* (14). Up to four *OPW* are needed in order to describe properly the valence wave function at that point (17). Figure 13 shows the upper part of a binned 3×3 histogram. Depressions are clearly seen along diagonal lines with respect to the measured plane, at 2 mrad from the centre, corresponding to the *WUW* lines of the *BZ*.

Finally, we might conclude that this measurement is a solid proof for the reliability of our experimental system. By means of a purely phenomenological analysis the basic features of the momentum distribution in aluminum were revealed: its, already known, *FS* topology, including deviations from free electron behaviour; the core annihilation; the many body effects and the umklapp processes. It is evident that for a better quantitative agreement a direct computation of the momentum distribution is needed [14, 18].

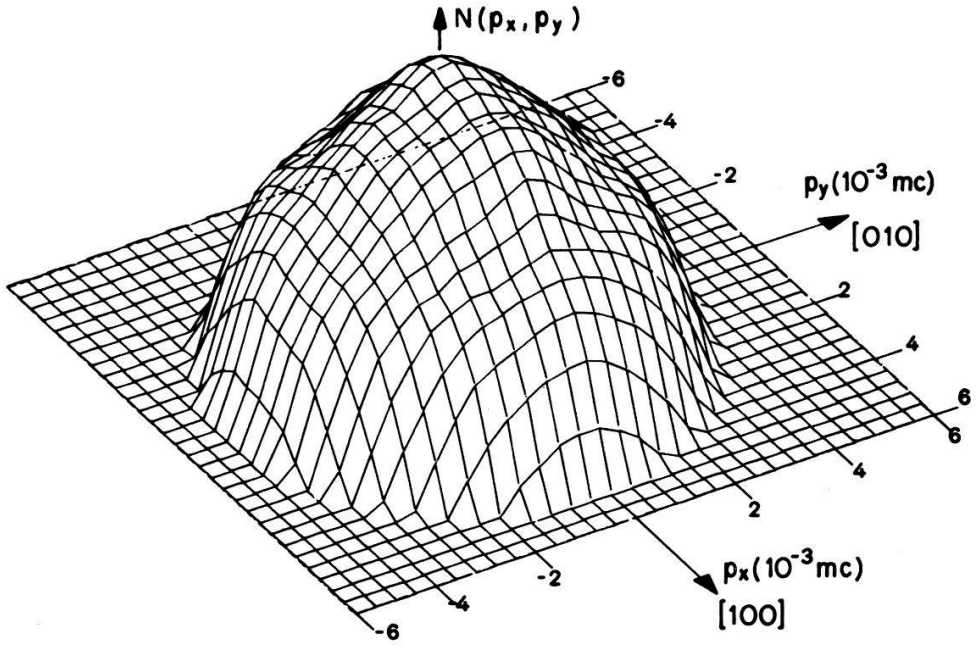

Figure 13
The upper part of a binned 3×3 histogram in aluminum. The observed depressions are attributed to the zone boundary interaction (see text).

2. *Copper*

Copper is a transition metal possessing the face centered cubic crystal structure and an electronic configuration of $(Ar)3d^{10}4s^1$. Its *FS* is well known due to precise de Haas Van Alphen (dHvA) measurements. It consists of a central ovoid, the belly, with eight necks in the [111] directions, touching the *BZ* at points *L*. Moreover, it can be described analytically by a Fourier series (19). The coefficients were determined by fitting dHvA experimental results.

As for previous positron annihilation experiment on copper, the reader shall refer to review articles (2) and to recently published works (20, 21).

The single crystals (6) for the two performed measurements (22) were grown from the melt using the Czochralski technique. The samples were cut by spark erosion, etched, annealed in vacuum at 950°C for 24 hours, slowly cooled and etched before measuring. Their dimensions were 10 mm long and 0.8 mm wide. Hence the effective angular resolution of 0.75×0.68 mrad^2 at 77 K is expected.

In the first measurement, the $(\bar{2}11)$ measurement, the crystallographic axis [111] and [110] were aligned along θ_x and θ_y respectively. In the second, the (111) measurement, θ_x and θ_y correspond to the [110] and $[\bar{2}11]$ axes. Figure 14 shows the experimental results for both measurements, the corresponding crystallographic configurations and model reconstructions. The *FS*, obtained from Halse's parametric equation (19), is superimposed on a Gaussian 2-*D* distribution representing the core annihilation. The qualitative agreement between experiment and the computed model is striking. In the $(\bar{2}11)$ measurement the top of the distribution is flat due to the relative position of two close necks at $\theta_y = 0$ and $\theta_x = \pm 1.6$ mrad. In the [111] measurement those two necks coincide at $\theta_x = \theta_y = 0$ and contribute to the well resolved outgrowth at the top. The isodensity contour lines mappings of those distributions are shown in Fig. 15. They reveal the positions of the remaining 6 necks of the copper *FS*. Thus, in both measurements

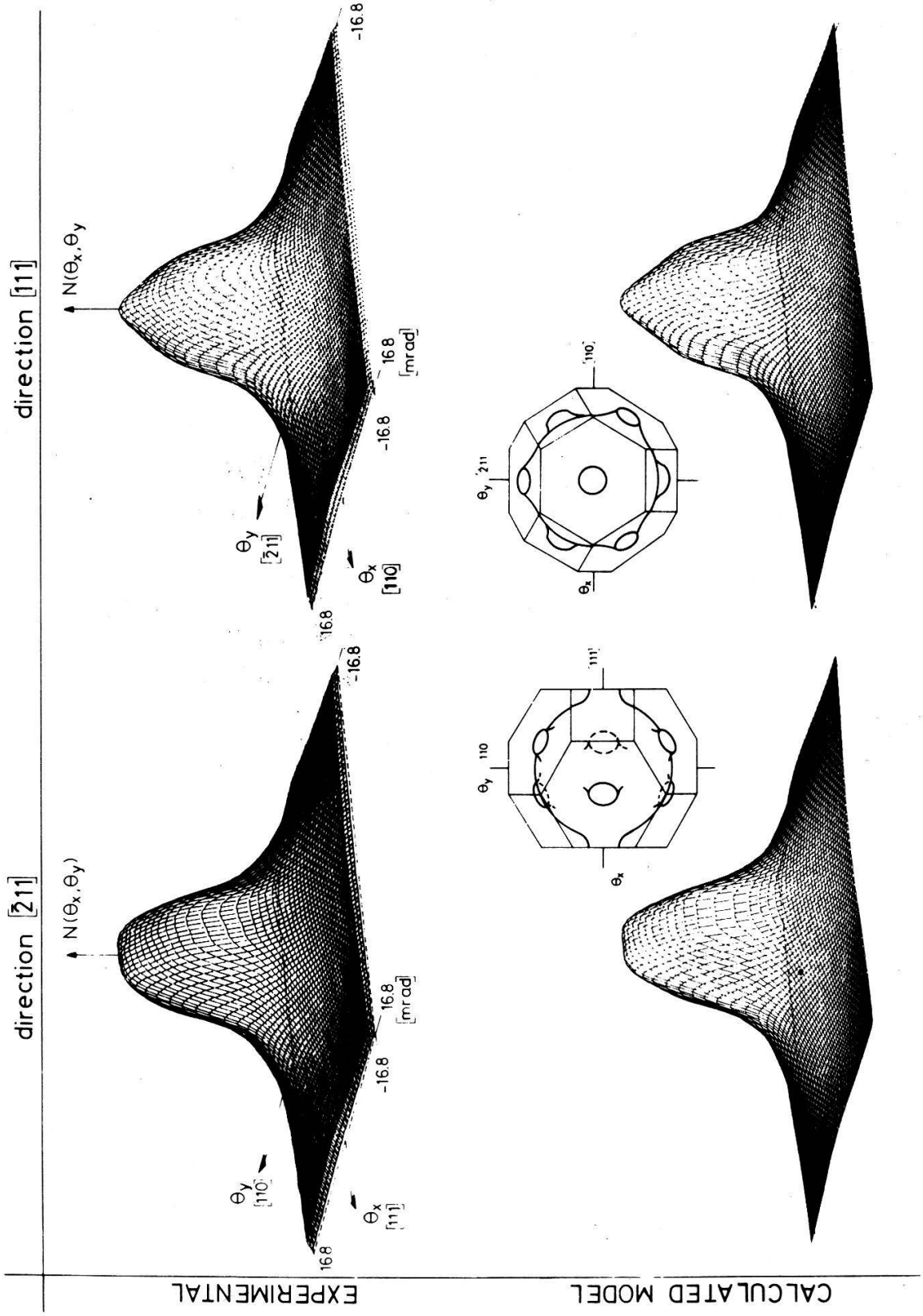

Figure 14
Experimental angular distribution in copper for two crystallographic configurations and model reconstructions. The histograms are binned 2×2, the spacing is 0.396 mrad in both directions.

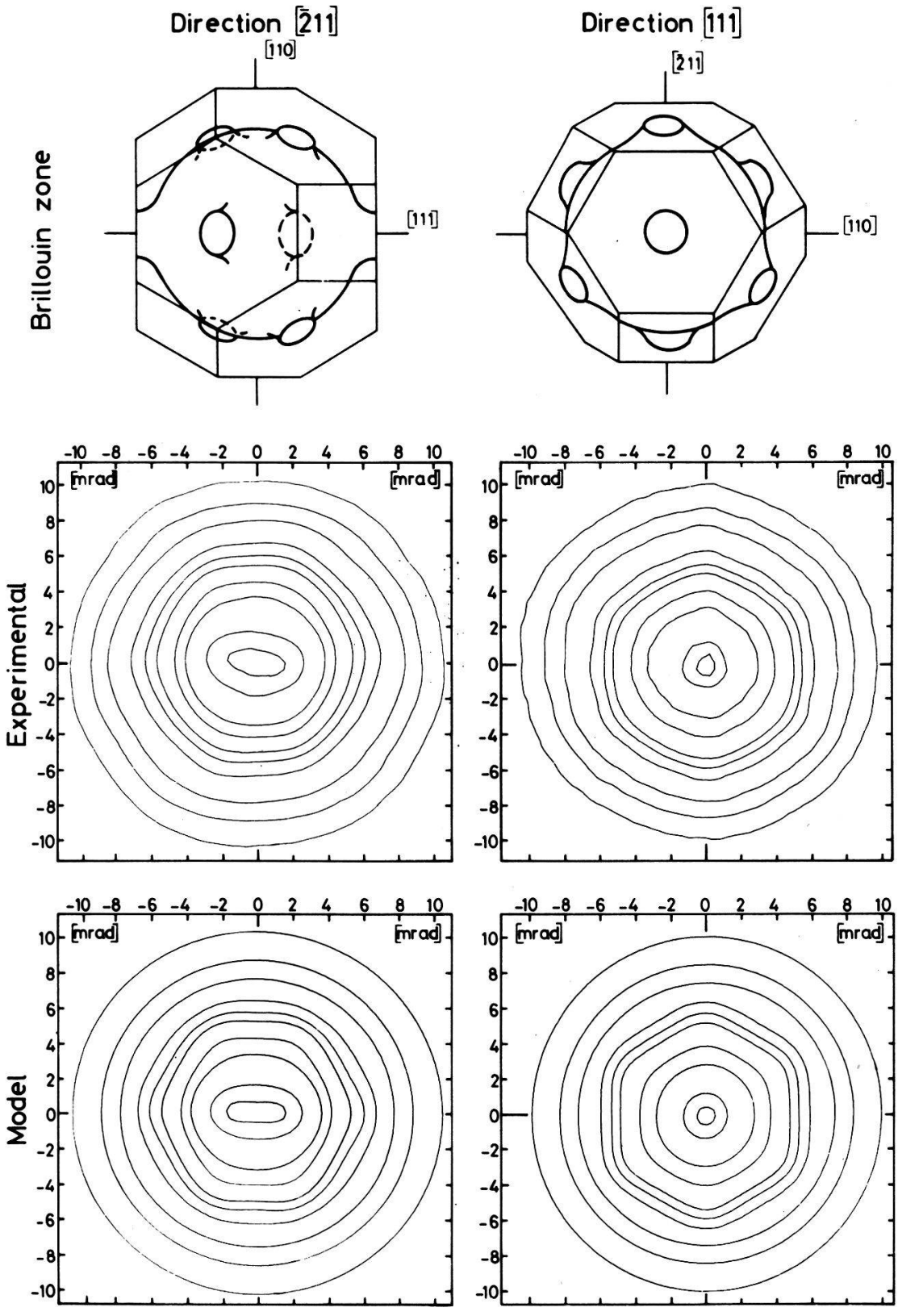

Figure 15
Isodensity contour lines mappings of the distributions of Fig. 14.

the detailed topology of the *FS* is unambiguously detected and in agreement with dHvA results.

A quantitative estimate of the neck dimension (23) might be obtained from the [111] measurement. Figure 16 shows the projective representation and the isodensity contour lines mapping of the partial derivatives $|\partial N(\theta_x, \theta_y)/\partial\theta_x|$. The neck manifests itself by the hill structure at the centre or by the strong deviation of the contour lines near that point. The derivative $|\partial N(\theta_x, \theta_y)/\partial\theta_x|$ for $\theta_x = 0$, folded at $\theta_x = 0$ is shown in Fig. 17. The position of the maximum in that derivative suggests that the neck radius is 1.0 ± 0.1 mrad, in complete agreement with previous positron annihilation measurements [20, 24], as well as dHvA ones (25).

The umklapp contribution reflects itself at large angles. The isodensity contour lines mappings for both measurements, as well as the positions of the first

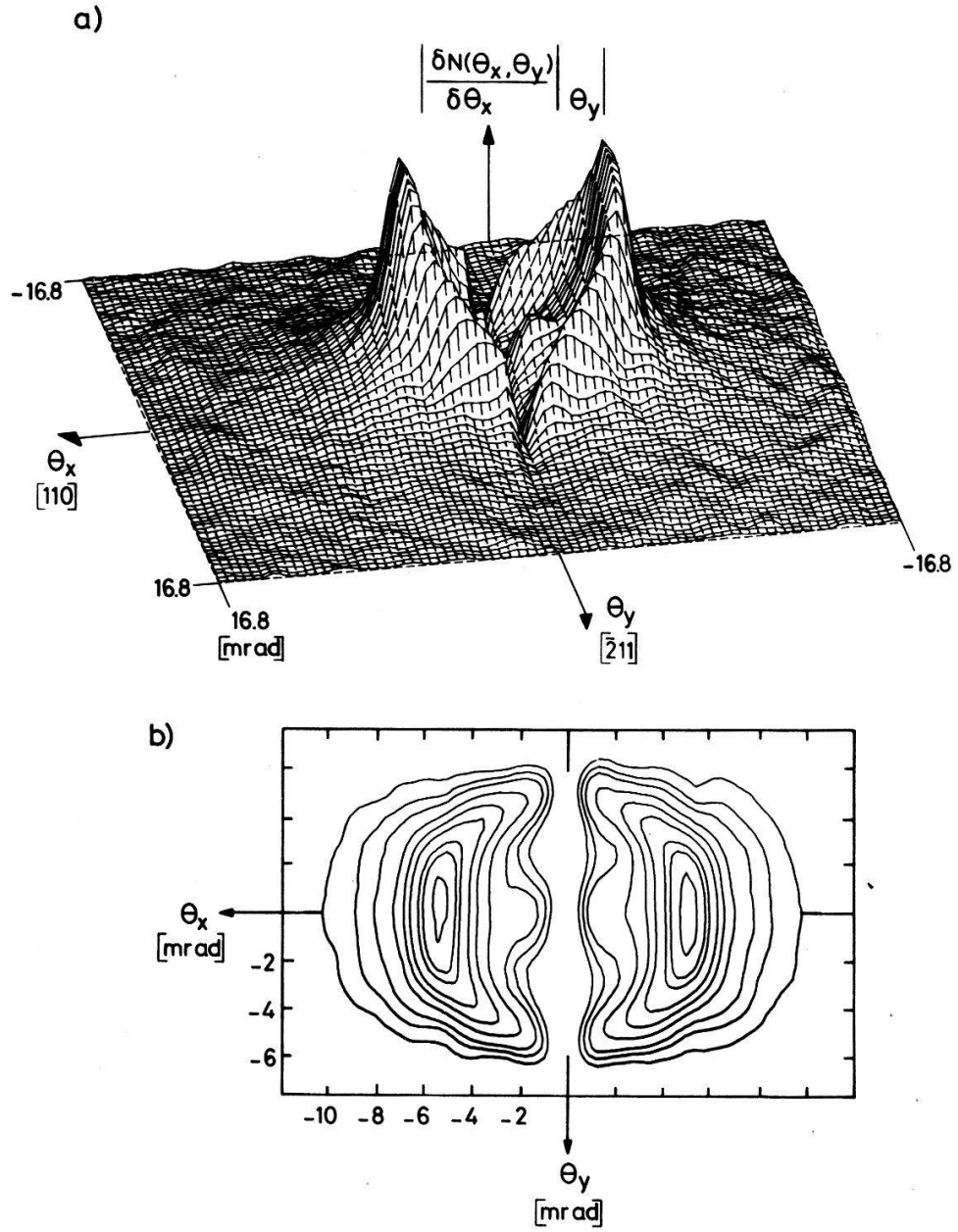

Figure 16
The projective representation and the isodensity contour lines mapping of the partial derivatives $|\partial N(\theta)/\partial\theta_x|$ for the (111) measurement in copper.

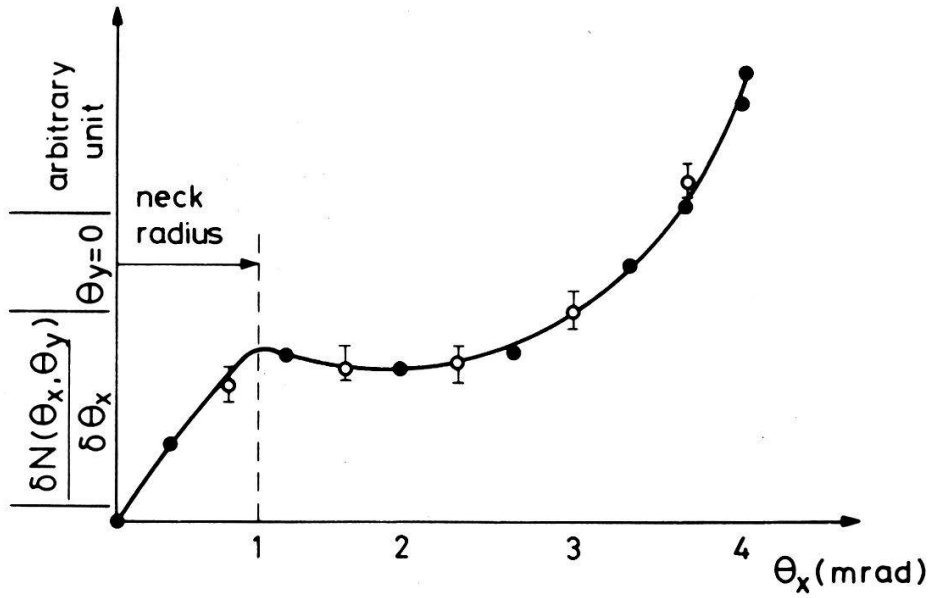

Figure 17
The partial derivative $|\partial N(\theta)/\partial\theta_x|$ for $\theta_x = 0$ and folded at $\theta_x = 0$, for the (111) measurement in copper. The empty points correspond to $\theta_x > 0$ and full ones to the folded values for $\theta_x < 0$.

BZ and the *NNBZ* are shown in Fig. 18. In both measurements the outer contour line exhibits deviations from a circle. The intensity is maximal at the centres of the *NNBZ* and minimal in between. A further confirmation for the *HMC* might be obtained from the projective representation of the partial derivatives $|\partial N(\theta_x, \theta_y)/\partial\theta_x|$ of the (111) measurement. It is shown in Fig. 19 amplified in intensity and truncated at the top. The rings at the bottom and around the central prominent part correspond to the positions of the outer edges of the *FS* centered at the *NNBZ* and exhibit the expected symmetry of the reciprocal lattice.

It is well known that the core annihilation in copper is the biggest contribution to the annihilation rate. Long-slit experiments normalized to 1 at $\theta = 0$ show

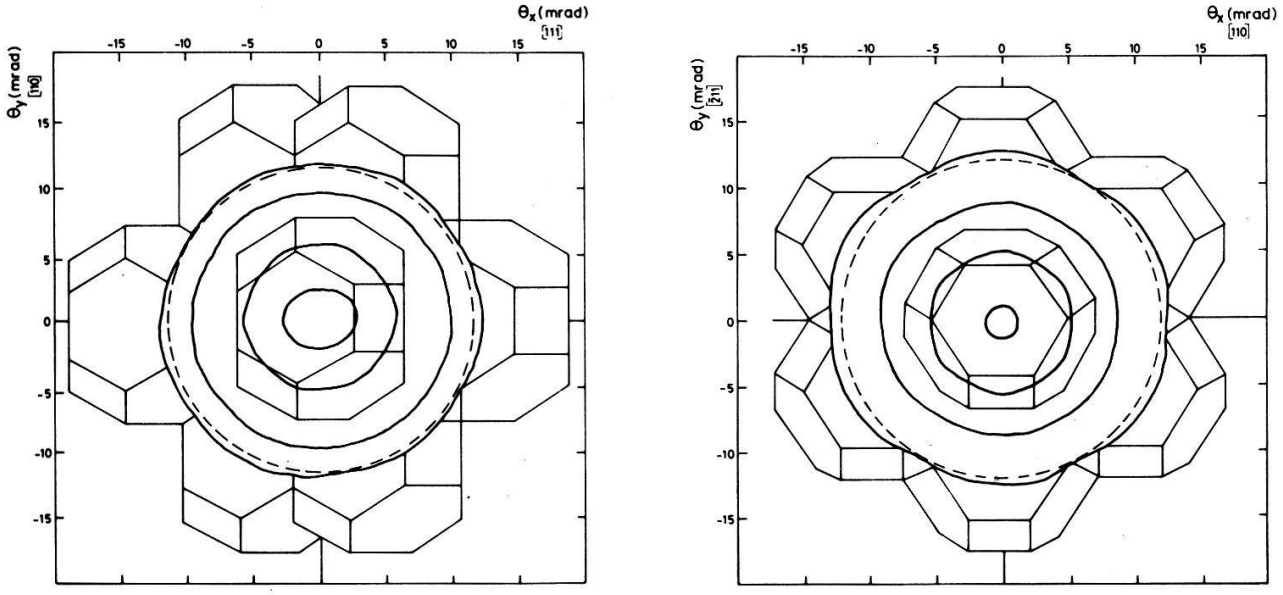

Fig. 18
Isodensity contour lines for both measurements in copper, exhibiting the *HMC* contribution. The positions of the 1st *BZ* and the *NNBZ* are indicated. The intensities are between 4% (the outer one) and 95% (the inner one) of the peak.

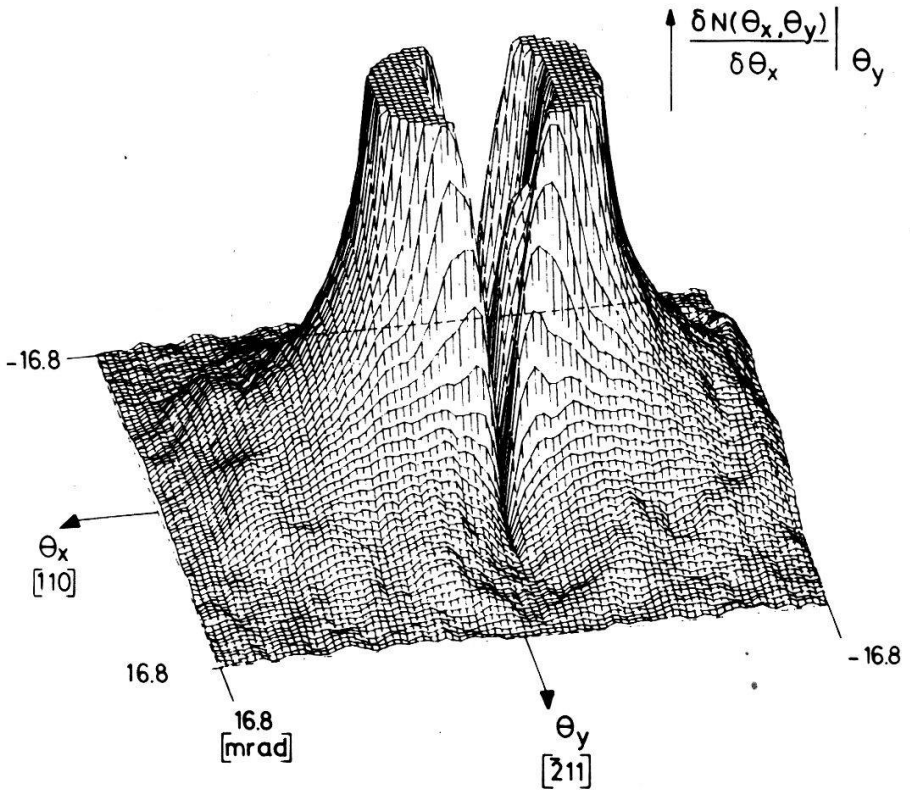

Figure 19
The partial derivatives $|\partial N(\theta)/\theta_x|$ of the (111) measurement in copper amplified in intensity and truncated at the top. The rings appearing in the bottom and around the central and prominent part are attributed to umlapp annihilations.

that its relative amplitude at that point is 0.6 ± 0.02 (26, 29) and that it exhibits long tails. This is mainly due to the fact that the valence wave function has a marked *s-d* character, therefore a smaller overlap with the wave function of the positron in the Wigner–Seitz cell. As for the momentum distribution of that contribution, it is usually represented by a Gaussian at large angles, but, at small angles, although experimental information is not lacking, there is not a general consensus.

We tried to obtain some information about that contribution from our 2-*D* measurements, using the *LSQF* method (Section A-5c). The theoretical model consisted of:

- A flat random coincidences contribution.
- The *FS* contribution obtained from the parametric equation of Halse. The many body effects were not considered since the Kahana type of enhancement, computed for a free electron gas, is not appropriate for copper. We shall return to that point later.
- The core annihilation contribution.

The many body effects and the umklapp processes are ignored in this model. The sum of the three considered contributions was convoluted with the experimental resolution.

As a first approximation we assumed that the core contribution can be represented by a single 2-*D* Gaussian function. The fit obtained was not satisfying and the χ^2 test pointed out that the model was not appropriate. A close examination of the residual spectrum of that fit revealed the presence of a ring

centered at the origin with a mean radius of about 6 mrad. Therefore, we tried a two-component model function of the core annihilation:

- A 2-*D* Gaussian centered at $\theta_x = \theta_y = 0$:

$$C_1 \exp(-x^2/2\sigma_x) \exp(-y^2/2\sigma_y)$$

- A ring having a Gaussian profile:

$$C_2 \exp(-(r-r_0)^2/2\sigma_r^2)$$

where $r^2 = x^2 + y^2$ and r_0 is the mean radius of the ring.

The theoretical fit with this new model function for the core contribution was acceptable and yielded the following results (experimental spectrum normalized to 1):

$$C_1 = 0.4 \pm 0.02 \qquad \sigma_x = \sigma_y = 7.5 \pm 0.3 \text{ mrad}$$

$$C_2 = 0.09 \pm 0.02 \qquad \sigma_r = 0.72 \pm 0.008 \text{ mrad} \qquad r_0 = 5.6 \pm 0.4 \text{ mrad}$$

The corresponding model function is shown in Fig. 20. The long-slit of the $(\bar{2}11)$ measurement in the [111] direction is shown in Fig. 21, as well as the core contribution. Those results are in agreement with the work of Senicki et al. (27) and they stress the non-Gaussian character of the core annihilation momentum distribution in copper.

As for the many body effects, we tried to shed some light on this question by substracting, in both measurements, the analytically known *FS* contribution from the experimental data, properly normalized and resolution taken into account. The result for the $(\bar{2}11)$ measurement is shown in Fig. 22, a similar result is obtained also from the (111) measurement. It is puzzling since an anisotropy appears and moreover is quite localized in the region of the necks. This distribution is the sum of the core annihilation, the *HMC* and the many body effects. The non-Gausian character of the core annihilation is clearly seen. But, although previous works pointed out that in copper the core contribution has a directional

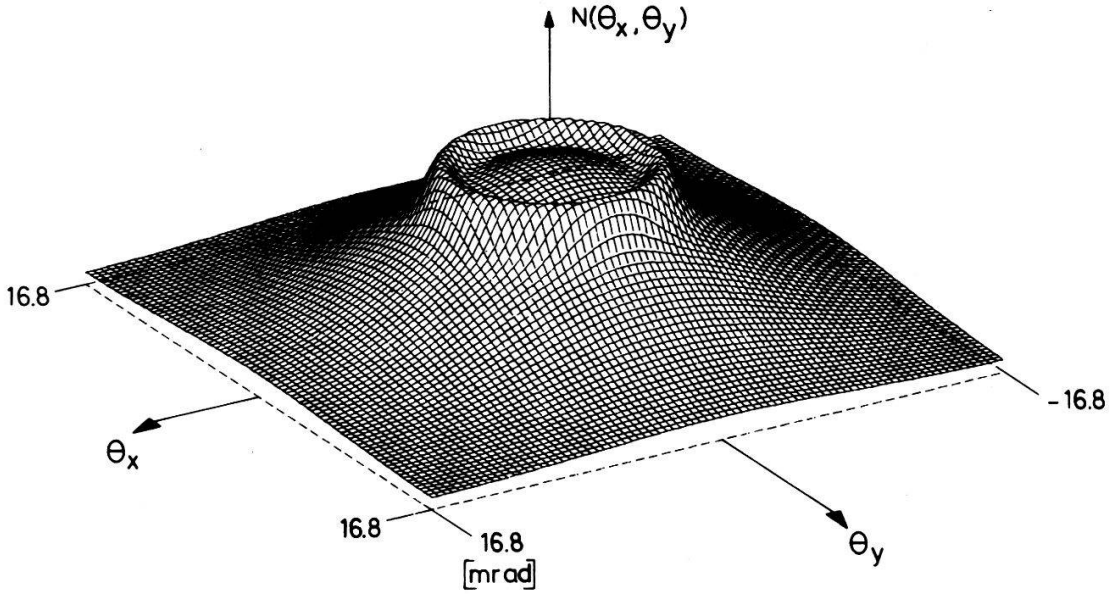

Figure 20
Model function for the core annihilation contribution in copper.

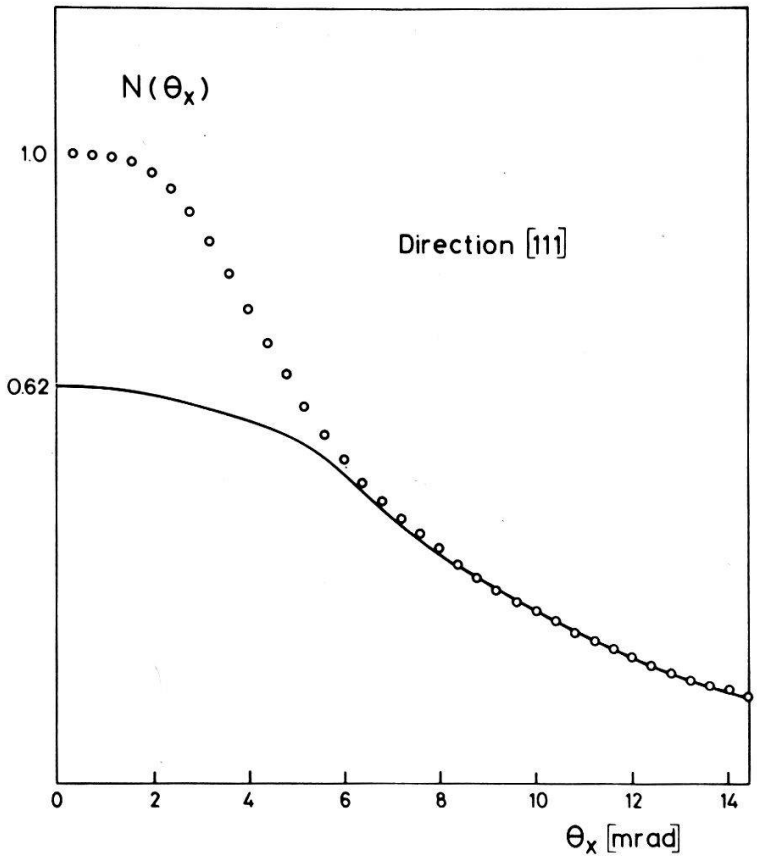

Figure 21
Simulated long-slit angular distribution of the ($\bar{2}11$) measurement in the [111] direction. The points represent experimental data and the full line is the core annihilation contribution corresponding to the model function of Fig. 19.

anisotropy (27), the striking feature is its localization. Three plausible reasons might be at the source of the observed anistropy. An *HMC* contribution, a band structure effect or a different many body interaction for *s* and *d* electrons. At first sight it seems that the *HMC* are weak, however they cannot be excluded completely. As for the other two, they are somehow related to the *s*-*d* hybridization of the electronic wave function in copper. Experimentally the anisotropy

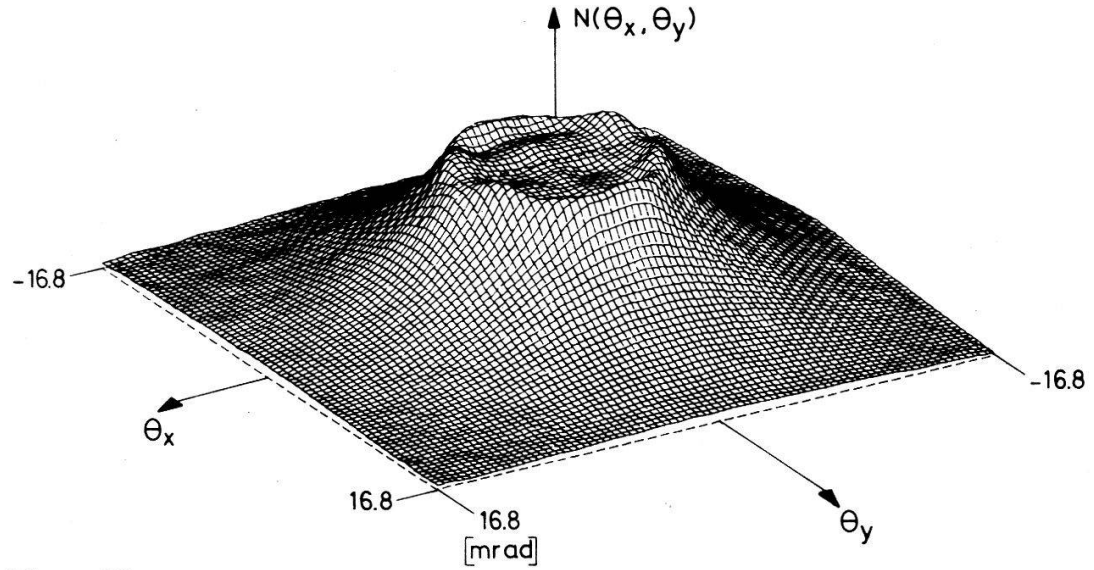

Figure 22
The experimental angular distribution of the ($\bar{2}11$) measurement after substraction of the *FS* contribution.

appears in the region of the necks and theoretically it is computed that the partial d-density of states at the FS is about 50% of the total (30). At present, we cannot distinguish between the three possibilities. A theoretical approach (18) should be used rather than a phenomenological one.

Conclusion

We have presented in this work a bidimensional positron annihilation system. It is equipped with the newly conceived high density proportional chambers, characterized by a good spatial resolution. Although the properties of aluminum and copper are well known, the experiments on these metals demonstrated the potential of 2-D measurements. For instance, the deviations from free electron behaviour in aluminum and the anisotropic core momentum distribution in copper. These results encourage us to endeavour further experiments on more complicated or new compounds. We believe that this method will give useful information, particularly for those compounds whose electronic properties are difficult to investigate by other experiments.

Acknowledgements

This work profited from the technical assistance of Mr. K. Kull of the C.E.R.N., in the construction of the detectors and of Dr. Sachot for his advices during the operational tests of the experimental setup. Their help is gratefully appreciated.

Our work also benefited from Dr. Walker's assistance and interest in the crystal growth of the samples.

The authors would like to thank Prof. G. Wanner of the department of mathematics of the University of Geneva, for putting at their disposal his computer for the three dimensional visualities of a two-dimensional function.

The first author is grateful to Dr. T. Streater of the C.E.R.N. for his constant help in the software development of the operating system for our computer.

This work was supported by the Swiss National Science Foundation.

REFERENCES

[1] S. Berko and J. S. Plaskett, phys. Rev. *112*, 1877 (1958); A. T. Stewart and L. O. Roellig, Positron annihilation, Academic Press 1967, N-Y.

[2] R. N. West, Adv. in Phys. *23*, 266 (1973); S. Berko, Compton Scattering, edited by W. Brian, McGraw-hill 1977 p. 273–322.

[3] G. E. Lee-Whiting, Phys. Rev. *97*, 1557 (1955); J. P. Carbotte and H. L. Arora, Can. Journal of Phys. *45*, 387 (1967); A. Perkins and J. P. Carbotte, Phys. Rev. *B1* 101 (1970).

[4] S. Kahana, Phys. Rev. *129*, 1622 (1963); J. P. Carbotte and S. Kahana, Phys. Rev. *139*, A213 (1965).

[5] S. Berko, M. Hoghooie and J. J. Mader, Phys. Lett. *63A*, 335 (1977); A. A. Manuel, Ø. Fischer, M. Peter and A. P. Jeavons, Nucl. Inst. and Meth. *156*, 67 (1978).

[6] A. A. Manuel, Ph.D. Thesis No 1889, Geneva University, Switzerland, 1978.

[7] A. P. Jeavons, C. Cate, IEEE Trans. Nucl. Sc. *23*, 640 (1976); A. P. Jeavons, D. W. Townsend, N. L. Ford, K. Kull, A. A. Manuel, Ø. Fischer and M. Peter, IEEE Trans. Nucl. Sc. *25*, 164 (1978).

[8] A. P. JEAVONS, G. CHARPAK and K. J. STUBBS, Nucl. Inst. and Meth. *124*, 491 (1975).
[9] G. CHARPAK, D. RAHM and H. STEINER, Nucl. Inst. and Meth. *80*, 13 (1970).
[10] W. BRANDT, Appl. Phys. *5*, 1 (1974).
[11] A. T. STEWART, J. B. SHAND and S. M. KIM, Proc. Phys. Soc. *88*, 1001 (1966).
[12] R. J. DOUGLAS and A. T. STEWART, Paper H14, 4th Int. Conf. Pos. Ann. Helsingor, Denmark 1976.
[13] Y. KUBO, S. WAKOH, J. YAMASHITA, J. Phys. Soc. of Japan *41*, 830 (1976); T. OKADA, H. SEKIZAWA, N. SHIOTANNI, J. Phys. Soc. of Japan *41*, 836 (1976).
[14] J. J. MADER, S. BERKO, H. KRAKAUER and A. BANSIL, Phys. Rev. Lett. *37*, 1232 (1976).
[15] E. DANIEL and S. H. VOSKO, Phys. Rev. *120*, 2041 (1960).
[16] P. KUBICA and A. T. STEWART, Phys. Rev. Lett. *34*, 852 (1975).
[17] N. W. ASHCROFT, Phil. Mag. *8*, 2055 (1963).
[18] P. E. MIJRANENDS, Physica *63*, 235 (1958); R. HARTHOORN and P. E. MIJRANENDS, J. Phys. *F8*, 1147 (1978).
[19] F. G. MOLINER, Phil. Mag. *3*, 207 (1958); D. J. ROAF, Phil. Trans. Roy. Soc. Lon. *A250*, (1962); M. R. HALSE, Phil. Trans. Roy. Soc. Lond. *A269*, 507 (1969); P. BOSACCHI and P. FRANZONI, J. Phys. *F6*, L99 (1976).
[20] S. BERKO and J. J. MADER, Appl. Phys. *5*, 287 (1975).
[21] M. HAGHOOGIE, J. J. MADER and S. BERKO, Phys. Lett *69A*, 293 (1978).
[22] A. A. MANUEL, S. SAMOILOV, Ø. FISCHER, M. PETER and A. P. JEAVONS, J. DE PHYS. C6 *39*, 1084 (1978).
[23] A. A. MANUEL, S. SAMOILOV, Ø. FISCHER, M. PETER and A. P. JEAVONS, Helv. Phys. Acta *52*, 37 (1979).
[24] K. FUJIWARA and O. SUEOKA, J. Phys. Soc. of Japan *21*, 1947 (1966).
[25] A. S. JOSEPH, A. C. THERSEN, E. GERTNER and L. E. VALBY, Phys. Rev. *148*, 569 (1966).
[26] J. MELNGAILIS, Phys. Rev. *B2*, 563 (1970).
[27] E. D. M. SENICKI, E. H. BECKER, A. G. GOULD and B. G. HOGG, Phys. Rev. Lett. *41A*, 293 (1972); E. D. M. SENICKI, E. H. BECKER, A. G. GOULD, R. N. WEST and B. G. HOGG, J. Phys. Chem of Solids *34*, 673 (1973).
[28] B. ROZENFELD, S. CHABIK, J. PAJAK, K. JERIE and W. WIERZCHOWSKY, Acta Phys. Polonica *A44*, 21 (1973).
[29] D. G. LOCK and R. N. WEST, Appl. Phys. *6*, 249 (1975).
[30] O. JEPSEN, D. GLOTZEL and A. R. MACINTOSH, to be published.